Bacterial detection by NAIP/NLRC4 elicits prompt contractions of intestinal epithelial cell layers

Pilar Samperio Ventayol[a], Petra Geiser[a], Maria Letizia Di Martino[a], Alexandra Florbrant[a], Stefan A. Fattinger[a,b], Naemi Walder[b], Eduardo Sima[c], Feng Shao[d], Nelson O. Gekara[e], Magnus Sundbom[c], Wolf-Dietrich Hardt[b], Dominic-Luc Webb[f], Per M. Hellström[f], Jens Eriksson[a], and Mikael E. Sellin[a,1]

[a]Science for Life Laboratory, Department of Medical Biochemistry and Microbiology, Uppsala University, 75123 Uppsala, Sweden; [b]Institute of Microbiology, Department of Biology, ETH Zürich, 8093 Zürich, Switzerland; [c]Department of Surgical Sciences, Uppsala University, 75185 Uppsala, Sweden; [d]National Institute of Biological Sciences, 102206 Beijing, China; [e]Department of Molecular Biosciences, The Wenner-Gren Institute, Stockholm University, Stockholm 10691, Sweden; and [f]Department of Medical Sciences, Gastroenterology and Hepatology Unit, Uppsala University, 75185 Uppsala, Sweden

Edited by Ralph R. Isberg, Tufts University School of Medicine, Boston, MA, and approved February 24, 2021 (received for review July 3, 2020)

The gut epithelium serves to maximize the surface for nutrient and fluid uptake, but at the same time must provide a tight barrier to pathogens and remove damaged intestinal epithelial cells (IECs) without jeopardizing barrier integrity. How the epithelium coordinates these tasks remains a question of significant interest. We used imaging and an optical flow analysis pipeline to study the dynamicity of untransformed murine and human intestinal epithelia, cultured atop flexible hydrogel supports. Infection with the pathogen *Salmonella* Typhimurium (*S*.Tm) within minutes elicited focal contractions with inward movements of up to ∼1,000 IECs. Genetics approaches and chimeric epithelial monolayers revealed contractions to be triggered by the NAIP/NLRC4 inflammasome, which sensed type-III secretion system and flagellar ligands upon bacterial invasion, converting the local tissue into a contraction epicenter. Execution of the response required swift sublytic Gasdermin D pore formation, ion fluxes, and the propagation of a myosin contraction pulse across the tissue. Importantly, focal contractions preceded, and could be uncoupled from, the death and expulsion of infected IECs. In both two-dimensional monolayers and three-dimensional enteroids, multiple infection-elicited contractions coalesced to produce shrinkage of the epithelium as a whole. Monolayers deficient for Caspase-1(-11) or Gasdermin D failed to elicit focal contractions but were still capable of infected IEC death and expulsion. Strikingly, these monolayers lost their integrity to a markedly higher extent than wild-type counterparts. We propose that prompt NAIP/NLRC4/Caspase-1/Gasdermin D/myosin–dependent contractions allow the epithelium to densify its cell packing in infected regions, thereby preventing tissue disintegration due to the subsequent IEC death and expulsion process.

bacterial infection | epithelium | organoid | inflammasome | contraction

Epithelial cells make up barriers that shield the interior of the body from the environment. In the homeostatic intestine, the surface of the epithelium is maximized to facilitate uptake of ingested nutrients, water, and electrolytes (1, 2). This large surface, however, makes the gut epithelium vulnerable to attack by pathogenic microorganisms. Pathogen onslaught and the ensuing inflammation causes death and loss of intestinal epithelial cells (IECs) (3, 4). This can be beneficial as damaged cells and intracellular pathogens are cleared from the mucosa. At the same time, cell loss may jeopardize epithelial integrity when insufficient IEC numbers remain to uphold the barrier. One way to prevent such an outcome would be to compact the epithelial layer in affected regions. It is well known that smooth muscle contraction results in shrinkage and compaction of the intestinal wall during inflammation (5), but whether and how the epithelium itself can alter its IEC packing upon infection appears less clear.

As a system to sense mucosal intrusions, IECs express pattern recognition receptors (PRRs) [e.g., Toll-like receptors associated with cell membranes (6), and Nod-like receptors (NLRs) that form inflammasomes in the cytosol] (7–9). Epithelial recognition of pathogens through PRRs elicits a panel of countermeasures, including production of proinflammatory cytokines, chemokines, lipids (10–13), secretion of antimicrobial peptides (11, 14), and the death and expulsion of infected IECs into the lumen (12, 15, 16). An intricate cross-talk exists between IECs and immune cells residing in the underlying lamina propria (17). Epithelial defense signaling has in some cases also been shown to engage bystander epithelial cells surrounding a pathogen-infected IEC (18–20). Still, it remains poorly explored how PRR recognition of invading pathogens can instruct tissue-scale epithelial responses.

Intestinal epithelial organoids (denoted "enteroids" when established from small intestinal crypts) provide a powerful experimental system to assess the behavior of untransformed epithelia in the absence of other mucosal cell types (21). Organoids can be grown as three-dimensional (3D) miniature organs within matrix domes (22, 23) or be disrupted to produce two-dimensional (2D) monolayers atop coated surfaces (24–27). By contrast to tumor cell lines, organoids maintain untransformed properties over time (28) and show reliable PRR expression patterns that mimic the intact gut

Significance

Contractile movements in the mammalian intestine typically rely on dedicated muscle cells. Here, we however show that untransformed intestinal epithelial cell layers initiate immediate focal contractions, affecting hundreds to thousands of epithelial cells, in response to bacterial infection. This epithelial contraction response occurs in the absence of other mucosal cell types. Instead, the epithelium itself senses the pathogen intrusion through a pattern recognition receptor complex—NAIP/NLRC4—and initiates actomyosin contractions that propagate across the epithelial layer. Within minutes, this response densifies the cell packing at infection sites and may prevent tissue disintegration during the subsequent stage of epithelial cell death and expulsion. Our results highlight a previously unappreciated dynamic behavior of intestinal epithelia.

Author contributions: P.S.V. and M.E.S. conceived the study; P.S.V., P.G., M.L.D.M., A.F., S.A.F., E.S., M.S., W.-D.H., D.-L.W., P.M.H., and M.E.S. designed research; P.S.V., P.G., M.L.D.M., A.F., S.A.F., N.W., E.S., and J.E. performed research; M.L.D.M., S.A.F., F.S., N.O.G., W.-D.H., and J.E. contributed new reagents/analytic tools; P.S.V., P.G., and A.F. analyzed data; P.S.V. and M.E.S. wrote the paper; and all authors reviewed and edited the paper.

The authors declare no competing interest.

This article is a PNAS Direct Submission.

[1]To whom correspondence may be addressed. Email: mikael.sellin@imbim.uu.se.

This article contains supporting information online at https://www.pnas.org/lookup/suppl/doi:10.1073/pnas.2013963118/-/DCSupplemental.

Published April 12, 2021.

epithelium (6, 9). Organoid models have for these reasons become attractive tools for physiological studies of gut infection (25, 29–32).

In this work, we used time-lapse imaging to follow the tissue dynamicity of enteroid-derived mouse and human intestinal epithelia, placed atop pliable matrix supports. Upon infection with the prototypical enteropathogen *Salmonella enterica* serovar Typhimurium (*S*.Tm), we observed prompt and large epithelial contraction foci which preceded and could be uncoupled from IEC death and expulsion. Bacterial type-three secretion system (TTSS) and/or cytosolic flagellin triggered the epithelial NAIP/NLRC4 inflammasome, sublytic Gasdermin D pore formation, ion fluxes, and myosin-dependent contractions spreading from sensing events at focal epicentres. We show that this swift response allows the epithelium to increase its IEC packing at sites of infection, which may minimize the disruptive effects of subsequent cell death and expulsion.

Results

S.Tm Infection Triggers Prompt Focal Contractions in Murine IEC Monolayers. To explore epithelial tissue dynamics upon infection, we developed enteroid-derived epithelial 2D-monolayers placed atop a flexible hydrogel in live-imaging chambers [informed by (26); see *SI Appendix*, *Materials and Methods*]. C57BL/6J mouse jejunal enteroids were first kept in 3D-culture containing CHIR99021 (CHIR, a glycogen synthase kinase-3 inhibitor) and valproic acid (VPA) to maximize proliferative potential (33, 34). Enteroids were subsequently fragmented into single cells, seeded out onto collagen-1 hydrogels, and the CHIR/VPA eliminated 24 h postseeding. IECs quickly attached to the hydrogel and extensive proliferation was noted during the first 24 to 48 h (Fig. 1 *A–D*). By 72 h, a postmitotic confluent epithelial monolayer was established (Fig. 1 *A–D*), which maintained at 96 h (Fig. 1*C*), and thereafter gradually deteriorated. The mature monolayer expressed low transcript levels of the stem cell marker Lgr5 (Fig. 1*E*), elevated levels of the differentiated enterocyte markers alkaline phosphatase and Ezrin (Fig. 1*E*), and featured a standing IEC arrangement with adherence junctions (E-cadherin) and an apical actin brush border (Fig. 1*F*).

To assess the impact of bacterial infection, we challenged mature IEC monolayers atop hydrogels with wild-type (WT) *S*.Tm SL1344 ("*S*.Tm^{wt}") at a multiplicity-of-infection (MOI) of 0.2-2 and imaged them by time-lapse differential interference contrast (DIC) microscopy. Strikingly, within 10 to 20 min postinfection (p.i.), large contraction foci became visible (Movie S1). We employed an optical flow image analysis pipeline to quantify the speed and direction of these epithelial movements [Movies S2 and S3 and Fig. 1*G*) (35); see *SI Appendix* for details]. Speed maps calculated from vector fields showed that each focus involved a 0.21 ± 0.14 mm^2 patch of epithelium (i.e., ~200 to 1700 IECs; Fig. 1 *H* and *I*), contracting toward a single epicentre with inward movements typically lasting 1.2 ± 0.3 min and maximal pixel speeds ranging between ~2 and 8 μm/min (Fig. 1 *G* and *J*). Early upon infection, isolated foci were readily detectable (Fig. 1*H*, 13 min p.i.), which subsequently coalesced into a patchwork (Fig. 1*H*, 23 min p.i.). Signs of epithelial cell death (rounding and dislodging of IECs) became evident thereafter, and contractile movements eventually ceased (Fig. 1*H*, 83 min p.i.). Infection-elicited contractions were also observed upon inoculation with another *S*.Tm^{wt} isolate (ATCC 14028s) (*SI Appendix*, Fig. S1 *A* and *B*) and in monolayers from a donor mouse housed in another facility (*SI Appendix*, Fig. S1 *C* and *D*). Exceedingly rare and small contraction foci could in fact occasionally be observed also prior to infection (Fig. 1 *I* and *J*). From this we conclude that murine IEC monolayers are wired to elicit prompt focal contractions upon *S*.Tm infection.

S.Tm TTSS-1 Docking and Invasion Elicits Focal Epithelial Contractions. *S*.Tm employs flagella and TTSS-1 to reach and invade the epithelium (36–38). Using fluorescence-labeled bacteria, we noted that contraction foci emerged in areas with *S*.Tm bound to the epithelial surface (Fig. 2*A*). This led us to postulate that *S*.Tm docking or invasion elicits focal contractions. To test this hypothesis, we infected murine monolayers with *S*.Tm^{wt} or *S*.Tm$^{\Delta invG}$ (lacks a structural component of TTSS-1). As expected, *S*.Tm^{wt} invaded IECs, while *S*.Tm$^{\Delta invG}$ failed to do so (*SI Appendix*, Fig. S1 *E* and *F*). Live DIC imaging over a range of MOIs (0.2 to 20) showed that epithelial contractions increased in frequency and intensity with *S*.Tm^{wt} dose (Fig. 2*B*). By sharp contrast, *S*.Tm$^{\Delta invG}$ infection did not elicit epithelial contractions, not even at the highest MOI (Fig. 2*B*). This points to a central role for TTSS-1 in triggering *S*.Tm-induced epithelial contractions.

TTSS-1 docks to the host cell membrane via a SipBC translocon, resulting in the transfer of TTSS-1-effectors into the host cell (39). Among the effectors, SipA stabilizes actin filaments, while SopB, SopE, and SopE2 drive actin filament nucleation through Rho and Arf GTPases (40). These four effectors largely explain TTSS-1–dependent host cell invasion both in vivo and in tissue culture models (38, 41). We used single- and multiple-effector mutant bacteria to assess the relationship between *S*.Tm IEC docking, invasion, and epithelial contraction. As evident in Fig. 2*C*, deletion of SipA (*S*.Tm$^{\Delta sipA}$), or the combined deletion of SopB, SopE, and SopE2 (*S*.Tm$^{\Delta sopBEE2}$), delayed the contraction response. Importantly however, even a strain lacking all four effectors (i.e., *ΔsipAsopBEE2*; "*S*.Tm$^{\Delta 4}$") elicited contractions which exceeded those of *S*.Tm$^{\Delta invG}$-infected monolayers (Fig. 2*C*). Hence, TTSS-1 docking to the epithelium suffices to elicit focal epithelial contractions, and TTSS-1 invasion effectors augment this effect.

NAIP/NLRC4 Sensing of the Infection at Contraction Focus Epicenters. An epithelial NAIP/NLRC4 inflammasome can sense bacterial ligands (TTSS rod and needle proteins, flagellin), trigger IEC death, and restrict bacterial spread to deeper tissues in vivo (12, 16, 42). To examine if the epithelial contraction response might be linked to NAIP/NLRC4, we generated enteroids from *Nlrc4*$^{-/-}$ (43) and *Villin*^{rfp}*Naip1-6*$^{\Delta/\Delta}$ mice (lacking all NAIP receptors and expressing a red fluorescent protein (RFP) reporter; see *SI Appendix*, *Materials and Methods*) and established monolayers atop hydrogels for infection. In side-by-side experiments, WT control monolayers again reacted to *S*.Tm^{wt} by vigorous contractions (Fig. 3 *A–D*). This response was, however, completely abolished in both *Nlrc4*$^{-/-}$ (Fig. 3 *A* and *B*) and *Villin*^{rfp}*Naip1-6*$^{\Delta/\Delta}$ (Fig. 3 *C* and *D*) monolayers across all MOIs tested. In fact, NLRC4- or NAIP-deficient monolayers appeared as refractory as WT monolayers infected by *S*.Tm$^{\Delta invG}$ (compare Figs. 3 *A* and *C* and 2*B*).

The involvement of NAIP/NLRC4 in epithelium contraction (Fig. 3 *A–D*) could be explained by several models. In the simplest one, NAIP/NLRC4 activation in an infected IEC initiates the contraction response with that cell at the epicenter. Alternatively, NAIP/NLRC4 might fuel propagation of contraction across the tissue following its initiation by other means. To resolve these possibilities, we established genetically chimeric IEC monolayers. 3D-enteroids were generated from WT and *Villin*^{rfp}*Naip1-6*$^{\Delta/\Delta}$ mice, the enteroids fragmented, and the fragments mixed in equal proportions before seeding atop hydrogels. This resulted in the outgrowth of confluent monolayers with alternating red *Naip1-6*$^{\Delta/\Delta}$ and noncolored WT regions (Fig. 3*E*). The chimeric monolayers were infected with *S*.Tm^{wt}, contraction foci tracked by time-lapse DIC imaging, and the epicenter locations overlaid with the RFP-fluorescence channel (Fig. 3*E* and Movie S4). Strikingly, contraction epicenters mapped virtually exclusively onto noncolored WT regions (>95% of epicenters; Fig. 3*E* and Movie S4). Following

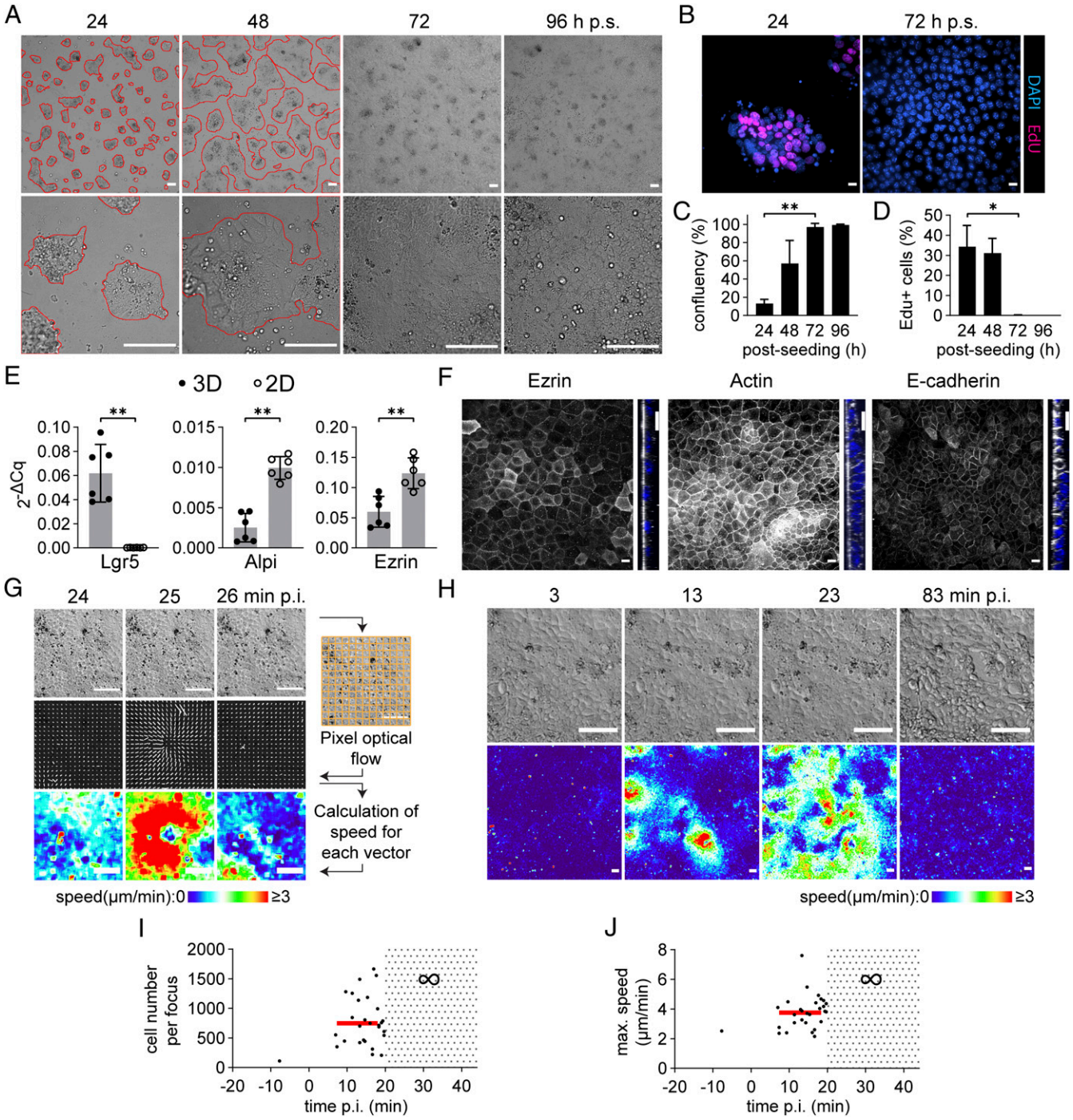

Fig. 1. *S*.Tm elicits prompt focal contractions in nonconstrained murine IEC monolayers. (*A–F*) Characterization of murine IEC monolayers atop hydrogels. (*A*) Murine enteroids were disrupted into single cells and seeded over a collagen-1 hydrogel. Depicted are representative DIC images at the indicated time points (hours postseeding; h p.s.) at low (*Top*) and high (*Bottom*) magnification. Red lines indicate borders of IEC islands. (Scale bars, 100 µm.) (*B*) Representative micrographs of monolayers (as in *A*) incubated with EdU (magenta). Nuclei visualized by DAPI (blue). (Scale bars, 10 µm.) (*C*) Quantification of monolayer confluence (as in *A*) and *D*) percentage EdU-positive IECs (as in *B*) over time. Data in *C–D* presented as mean ± SD of at least three independent experiments up to 72h p.s. Kruskal Wallis with Dunn´s post hoc test and Benjamini-Hochberg correction, comparing against the 24h sample (**P* < 0.05; ***P* < 0.01). (*E*) Transcriptional profiles of 3D-enteroids and mature 2D-monolayers (72h p.s.). Data presented as mean ± SD of six biological replicates per condition, pooled from two separate experiments. Data points shown as filled (3D) or empty (2D) circles, two-tailed Mann–Whitney *U* test (***P* < 0.01). (*F*) Representative micrographs of monolayers (72h p.s.) stained for Ezrin (*Left*; white), Actin (*Middle*; white), E-cadherin (*Right*; white), and DAPI (nuclei; blue). Depicted are x-y (*Left*) and z projection (*Right*) micrographs of confocal Z-stacks. (Scale bars, 10 µm.) (*G*) Example of an *S*.Tm-elicited contraction focus and the framework for flow analysis (schematic in margin). Depicted are DIC images (*Top*) from the indicated time frames (min p.i.), with visualization of vector fields (middle row panels) and speed–color maps (bottom row panels) derived from Cellocity. (Scale bars, 100 µm.) (*H*) Representative time-lapse series of a monolayer infected with *S*.Tm^{wt} at MOI 2. Depicted are DIC images (upper row panels) and speed–color maps (bottom row panels) at the indicated time points. Data representative for >10 independent experiments. (Scale bars, 100 µm.) (*I*) Quantification of contraction focus (as in *G* and *H*) cell numbers, and (*J*) maximum speeds over time. Each black dot represents one contraction focus. Means depicted by red lines. Gray spotted area represents contraction patchwork (∞).

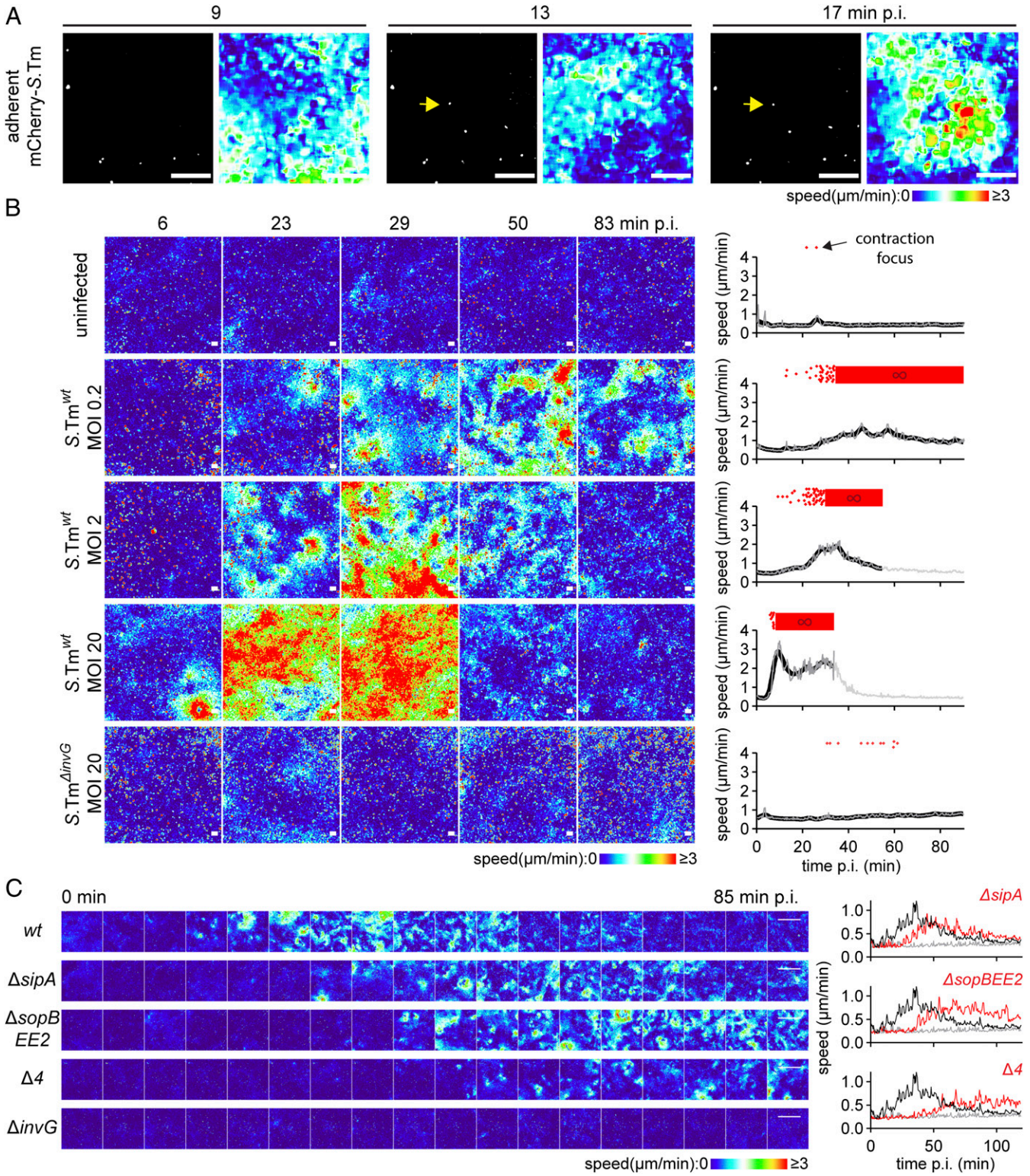

Fig. 2. *S*.Tm elicits focal epithelial contractions dependent on TTSS-1. (*A*) Representative time-lapse series of a murine IEC monolayer (as in Fig. 1*A*, 72h p.s.) infected with mCherry-*S*.Tm at MOI 0.2. Depicted are processed fluorescence images and speed–color maps at the indicated time points. Fluorescence channel background was corrected by addition of an inverse Gaussian blurred version of the image, and shown are means of five frames to visualize only nonmoving *S*.Tm (adherent; white). Yellow arrow indicates an *S*.Tm located at the contraction focus epicenter. (Scale bars, 100 µm.) (*B*) Speed–color maps of monolayers left uninfected or infected with *S*.Tm^{wt} or *S*.Tm$^{\Delta invG}$ at the indicated MOIs and time points. Graphs to the right show raw speeds for the whole field of view (f.o.v.) (gray) and local regression (black line) over time, stopping when monolayer integrity was compromised. Red dots atop graphs represent contraction foci over time. Red thick stripe represents contraction patchwork (∞). One representative experiment out of three is shown for each condition. (Scale bars, 100 µm.) (*C*) Speed–color maps of monolayers infected with *S*.Tm mutants deficient for TTSS-1 effectors SipA (Δ*sipA*), SopB, SopE, and SopE$_2$ (Δ*sopBEE2*), all four effectors combined (Δ*4*), or the structural component InvG (Δ*invG*). Graphs to the right show raw speeds for the whole f.o.v. upon infection with *S*.Tm^{wt} (black) and *S*.Tm$^{\Delta invG}$ (gray) (same data in all three graphs), plus the indicated mutant (red), over time. One representative experiment out of three is shown. (Scale bars, 1 mm.)

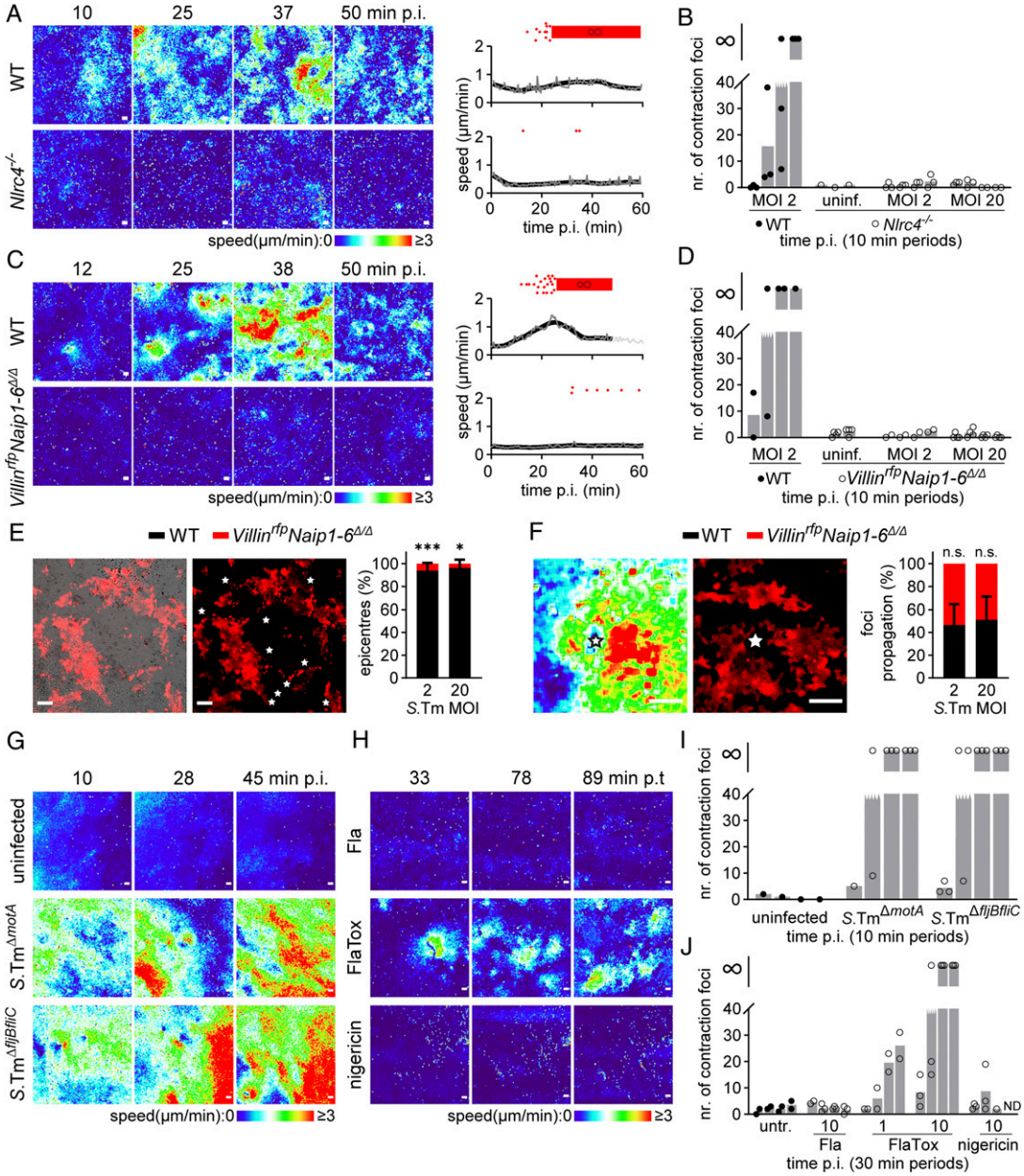

Fig. 3. Epithelial NAIP/NLRC4 sensing of bacterial ligands triggers focal contractions. (*A–D*) WT and either *Nlrc4*$^{-/-}$ (*A* and *B*) or *Villin*^{rfp}*Naip1-6*$^{\Delta/\Delta}$ (*C* and *D*) murine IEC monolayers (as in Fig. 1*A*, 72h p.s.) were infected in parallel with *S*.Tm^{wt} at the indicated MOIs. (*A*) Speed–color maps of infected WT and *Nlrc4*$^{-/-}$ monolayers (time points on top). Graphs to the right show raw speeds for the whole f.o.v. (gray) and local regression (black line) over time, stopping when monolayer integrity was compromised. Red dots atop graphs represent single contraction foci over time. Red thick stripe represents contraction patchwork (∞). One representative experiment out of three is shown. (Scale bars, 100 μm.) (*B*) Quantification of contraction foci numbers in infected WT and *Nlrc4*$^{-/-}$ monolayers (as in *A*) in the 0 to 10, 10 to 20, 20 to 30, and 30 to 40 min time periods p.i. at the indicated MOIs (uninf; uninfected). Each dot represents one monolayer. Bars indicate means. The symbol "∞" represents contraction patchwork. Data pooled from two to three independent experiments. (*C*) Speed–color maps and graphs of infected WT and *Villin*^{rfp}*Naip1-6*$^{\Delta/\Delta}$ monolayers, depicted as in *A*. One representative experiment out of three is shown. (*D*) Quantification of contraction foci numbers in infected WT and *Villin*^{rfp}*Naip1-6*$^{\Delta/\Delta}$ monolayers (*C*), depicted as in *B*. Data pooled from two independent experiments. (*E* and *F*) Chimeric murine IEC monolayers derived from WT (noncolored) and *Villin*^{rfp}*Naip1-6*$^{\Delta/\Delta}$ enteroids (red) were infected with *S*.Tm^{wt} at MOI 2 through 20. (*E*) Representative fluorescence plus DIC overlay (*Left*) and fluorescence-only (*Right*) image from a time-lapse series of an infected (MOI 2) chimeric monolayer. Stars represent contraction focus epicenters. (Scale bar, 100 μm.) Graph to the right shows the localization of epicenters to WT (black) or *Villin*^{rfp}*Naip1-6*$^{\Delta/\Delta}$ (red) regions. Bars represent mean ± SD. Data pooled from four to five monolayers per MOI from two independent experiments, χ^2 test (*$P < 0.05$; ***$P < 0.001$). (*F*) Representative speed–color map (*Left*) and fluorescence image (*Right*) of a single contraction focus. Star represents the epicenter. (Scale bar, 100 μm.) Graph to the right shows the propagation of contraction foci over WT (black) or *Villin*^{rfp}*Naip1-6*$^{\Delta/\Delta}$ (red) regions, normalized to the relative area in the f.o.v. Bars represent mean ± SD. Data pooled from in total 53 contraction foci, analyzed from two independent experiments. Paired Mann–Whitney *U* test (n.s., nonsignificant). (*G*) Speed–color maps of WT monolayers left uninfected or infected with *S*.Tm$^{\Delta motA}$ or *S*.Tm$^{\Delta fljBfliC}$ at MOI 30 (time points on top). (*H*) Speed–color maps of WT monolayers treated with 10 μg/mL flagellin (Fla), 10 μg/mL FlaTox, or 10 μM nigericin (time points on top). In *G* and *H*, one representative experiment out of two is shown. (*I*) Quantification of contraction foci numbers in infected monolayers (as in *G*), depicted as in *B*. (*J*) Contraction foci numbers in treated monolayers (as in *H*) in the 0 to 30, 30 to 60, 60 to 90 and 90 to 120 min time periods p.t. at the indicated concentrations. Data in *I* and *J* pooled from two independent experiments. ND, not determined.

https://doi.org/10.1073/pnas.2013963118

their initiation, however, contractions propagated equally across *Villin*^{rfp}*Naip1-6*$^{\Delta/\Delta}$ and WT regions (Fig. 3*F*). These data support that NAIP/NLRC4 bacterial sensing at invasion sites triggers the focal contraction response.

We next assessed the impact of specific NAIP ligand(s). Epithelial contractions were elicited also by a *S*.Tm$^{\Delta fljBfliC}$ strain that lacks flagellin (Fig. 3 *G* and *I*; nonmotile but flagellated *S*.Tm$^{\Delta motA}$ used as control). Combined with the previous results (Fig. 2 *B* and *C*), this suggests that TTSS-1 is sufficient to elicit contractions. Nevertheless, delivery of *Legionella pneumophila* flagellin into the IEC cytosol by the N-terminal domain of *Bacillus anthracis* lethal factor ["FlaTox" (44, 45)] also elicited contractions, while extracellular Fla or the NLRP3 inducer nigericin failed to do so (Fig. 3 *H* and *J*). These findings are consistent with the fact that naïve murine IECs express little NLRP3 but significant levels of all NAIP receptors [i.e., NAIP1, 2, 5, and 6 (9)] and are therefore poised to elicit focal contractions upon sensing of either bacterial TTSS or flagellin ligands.

Gasdermin D Sublytic Pore Formation Sparks Myosin-Dependent Focal Contractions that Precede and Can Be Uncoupled from IEC Death and Expulsion. Activated NAIP/NLRC4 can in turn activate Caspase-1 or Caspase-8, leading to either Gasdermin D pore formation and subsequent lytic cell death ["pyroptosis" (46)] or apoptotic cell death, depending on the cellular context (12, 47). In the intestinal epithelium, this results in the expulsion of infected IECs into the lumen (12, 15, 16) and the release of proinflammatory mediators (12, 15). We used genetic and pharmacological approaches to probe the relationship between the epithelial contraction response and potential pathways downstream of NAIP/NLRC4.

The adaptor protein Apoptosis-Associated Speck-Like Protein Containing CARD (ASC) associates with activated NAIP/NLRC4 and links this inflammasome to Caspase-8 activation in IECs (12, 47). However, *S*.Tm^{wt} infection elicited focal contractions in both *Asc*$^{-/-}$ (43) monolayers and matched controls (*SI Appendix*, Fig. S2 *A* and *B*), hence excluding a primary involvement of this pathway. By sharp contrast, monolayers established from mice lacking Caspase-1 [*Casp1/11*$^{-/-}$ (48)] or Gasdermin D [*GsdmD*$^{-/-}$ (49)] did not exhibit epithelial contractions (Fig. 4 *A*–*D*) (i.e., in line with findings in NAIP/NLRC4–deficient monolayers). To examine if lytic IEC death downstream of Caspase-1/Gasdermin D might explain the focal contractions, infections were repeated in WT monolayers in the presence of the dye Draq7, which enters lysed cells. Tracing of fluorescence within contraction foci showed that Draq7-positive expelled IECs only became visible in some cases and always later than the focal contraction phase (Fig. 4 *E* and *F*). Moreover, pretreatment with the broad-spectrum Caspase-inhibitor Z-VAD-FMK drastically reduced IEC death upon *S*.Tm infection but did not impact early contractions (Fig. 4 *G*–*J*).

Neighboring epithelial cells form an actin purse string to help expel a dying epithelial cell from a cell layer [a process referred to as "extrusion" (50)]. It remained plausible that this phenomenon could be linked to the large focal contractions noted here. However, in the live cell tracing experiments, we only observed IECs expelling from the monolayer subsequent to the contraction phase (exemplified in Fig. 4*E*). Homeostatic removal of IECs in uninfected monolayers (known to involve a typical extrusion process) were also not accompanied by any contraction foci propagating across the surrounding tissue (*SI Appendix*, Fig. S3*A*). Most importantly, in Caspase-1(-11)–deficient monolayers, *S*.Tm still elicited expulsion of infected IECs, but not focal epithelial contractions, hence formally uncoupling these two phenomena from each other (*SI Appendix*, Fig. S3*B*). Finally, typical cell extrusion relies on Sphingosine-1-phosphate (S1P) signaling between neighboring IECs (51), but we found that *S*.Tm-induced focal contractions proceeded normally also in the presence of S1P biosynthesis inhibitors (*SI Appendix*, Fig. S3*C*).

Proinflammatory signaling occurs concomitant with the death of *S*.Tm-infected IECs and involves interleukin-18 and eicosanoid release (12, 15). Neutralization of IL-18 by saturation with IL-18–binding protein (IL-18BP) had no impact on the epithelial contraction response (*SI Appendix*, Fig. S4*A*), neither did preincubation of monolayers with eicosanoid synthesis inhibitors (*SI Appendix*, Fig. S4 *B* and *C*). Transfer of culture supernatants from infected monolayers to naïve monolayers failed to elicit any contraction foci (*SI Appendix*, Fig. S4*D*). We also assessed proinflammatory gene transcription and found that this occurred in both *S*.Tm^{wt}- and *S*.Tm$^{\Delta invG}$-infected monolayers (*SI Appendix*, Fig. S4*E*), whereas exclusively *S*.Tm^{wt}-infected monolayers produced contraction foci (Fig. 2). Taken together, these results suggest that NAIP/NLRC4–dependent focal epithelial contractions require minute quantities of active Caspase-1 and the pore-forming protein Gasdermin D (46), but precede and can be uncoupled from IEC death and lysis, the IEC extrusion process itself, and generalized proinflammatory signaling.

Work in macrophages has shown that early pore formation by a small number of Gasdermin D molecules causes immediate ion fluxes, which can be blocked by Gd^{3+} (in the form of Gadolinium chloride) (52). Strikingly, preincubation of WT monolayers with Gd^{3+} revealed a dose-dependent reduction in the number of *S*.Tm^{wt}-elicited contraction foci (Fig. 4*K*). A brief incubation with the Calcium chelator EGTA also markedly attenuated the contraction response (*SI Appendix*, Fig. S5 *A* and *B*). In epithelial cells, nonmuscle myosin II (hereafter simply "myosin") can respond to ion fluxes and is fundamental for force generation, force transmission at adherence junctions, and apical constriction (53). To inhibit myosin activity, blebbistatin was used, as previously reported by others (54). Short-term blebbistatin incubation did not affect the epithelial monolayer morphology nor the numbers of tissue-associated *S*.Tm or late-stage IEC death (*SI Appendix*, Fig. S5 *C*–*F*). However, at low dose (10μM), blebbistatin dramatically reduced the number of *S*.Tm-induced contraction foci, and at high concentration (50μM), contractile movements ceased entirely (Fig. 4*L* and *SI Appendix*, Fig. S5*G*). From these data, we conclude that early sublytic Gasdermin D pore formation results in ion fluxes and the swift propagation of focal myosin contraction pulse(s) across the epithelium.

Early Focal Contractions Densify Infected Epithelial Regions and May Prevent Subsequent Tissue Disintegration. To determine if infection-induced contractions are relevant also for human gut epithelia, human jejunal enteroids were established and 2D-monolayers cultured atop hydrogels (see *SI Appendix*, *Materials and Methods* for details). Imaging of *S*.Tm^{wt}-infected human monolayers kept in expansion medium revealed some subtle epithelial movements (Fig. 5*A*, *Upper*; compare with Fig. 2*B*). When the medium was exchanged for Wnt3a-deficient medium at the time of confluence, human monolayers adopted a more differentiated appearance (*SI Appendix*, Fig. S6 *A* and *B*). In response to infection, these human monolayers displayed more pronounced focal contractions (Fig. 5*A*, *Bottom* and Movie S5). It should be noted that contraction foci were still fewer, and the contraction events less vigorous, than in the murine monolayers. Notably, neither the human transformed cell line Caco-2 C2Bb1 nor the immortalized mouse cell lines m-ICc$_{12}$ produced contraction foci when placed atop hydrogels and infected with *S*.Tm (*SI Appendix*, Fig. S6 *C* and *D*). These results indicate that infection-elicited gut epithelial contraction is a response shared between species but only observed in untransformed epithelial models, and most potent in murine epithelia.

The appearance of multiple contraction foci, each affecting hundreds to thousands of IECs (Fig. 1 *H* and *I*), could have consequences for the compaction of the epithelial layer. We

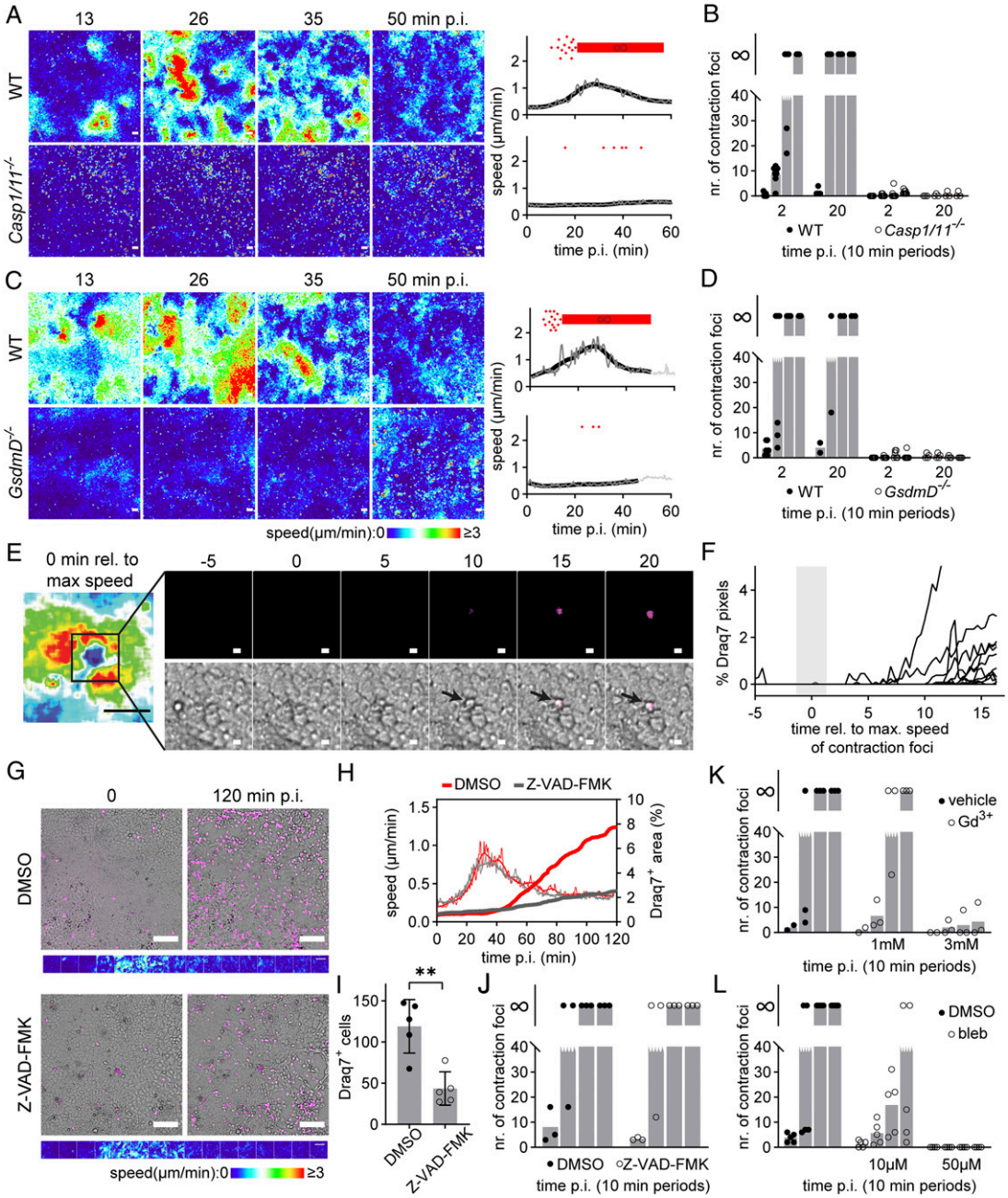

Fig. 4. Gasdermin D sublytic pore formation sparks myosin-dependent contractions. (*A*) WT and either *Casp1/11*$^{-/-}$ (*A* and *B*) or *GsdmD*$^{-/-}$ (*C* and *D*) murine IEC monolayers were infected with *S*.Tm^{wt} at the indicated MOIs. (*A*) Speed–color maps of infected WT and *Casp1/11*$^{-/-}$ monolayers infected at MOI 2 (time points on top). Graphs to the right show raw speeds for the whole f.o.v. (gray) and local regression (black line) over time, stopping when monolayer integrity was compromised. Red dots atop graphs represent single contraction foci over time. Red thick stripe represents contraction patchwork (∞). One representative experiment out of ≥3 shown. (Scale bars, 100 µm.) (*B*) Quantification of contraction foci numbers in infected monolayers as in A, in the 0 to 10, 10 to 20, 20 to 30, and 30 to 40 min time periods p.i. Each dot represents one monolayer. Bars indicate means. The symbol "∞" represents contraction patchwork. Data pooled from ≥3 independent experiments. (*C*) Speed–color maps and graphs of infected WT and *GsdmD*$^{-/-}$ monolayers at MOI 2, depicted as in *A*. One representative experiment out of ≥3 shown. (*D*) Quantification of contraction foci numbers in infected WT and *GsmdD*$^{-/-}$ monolayers (*C*), depicted as in *B*. Data pooled from ≥3 independent experiments. (*E* and *F*) Murine IEC monolayers were infected with *S*.Tm^{wt} at MOI 2 in the presence of Draq7. (*E*) Example of contraction focus at max speed (speed–color map, left) and image series (time relative to contraction) of the Draq7 channel (magenta, top row) and Draq7 channel merged with DIC (bottom row). Black arrows indicate an expelling IEC. (Scale bars, 100 µm, 10 µm in the time-lapse series.) (*F*) Quantification of Draq7 pixels within focal epicenters. Gray shading represents contraction focus duration. In total, 14 epicenters pooled from two independent experiments. (*G*) Representative time-lapse series of murine IEC monolayers infected with *S*.Tm^{wt} at MOI 2 in the presence of vehicle (DMSO) or 50µM Z-VAD-FMK and Draq7. Depicted are DIC plus fluorescence image overlays (upper row panels; Draq7 in magenta) and speed–color maps (bottom row panels; montage from 0 to 120 min p.i.). (Scale bars, 100 µm [*Top*] or 1 mm [speed–color maps].) (*H*) Quantification of the raw speeds for the whole f.o.v. (thin lines) and the total Draq7 signal area (thick lines) of monolayers as in *G*. (*I*) Quantification of Draq7-positive cells at 2 h p.i. in infected monolayers as in *G*. Each dot represents one monolayer. Bars indicate mean ± SD. Data pooled from two independent experiments, one-tailed Mann–Whitney *U* test (**$P < 0.01$). (*J*) Quantification of contraction foci numbers in monolayers as in *G*, depicted as in *B*. (*K* and *L*) Quantification of contraction foci numbers in infected monolayers treated with the indicated concentrations of *K* Gd^{3+} or *L* blebbistatin (bleb), depicted as in *B*. Data pooled from three (*K*) or five (*L*) independent experiments.

https://doi.org/10.1073/pnas.2013963118

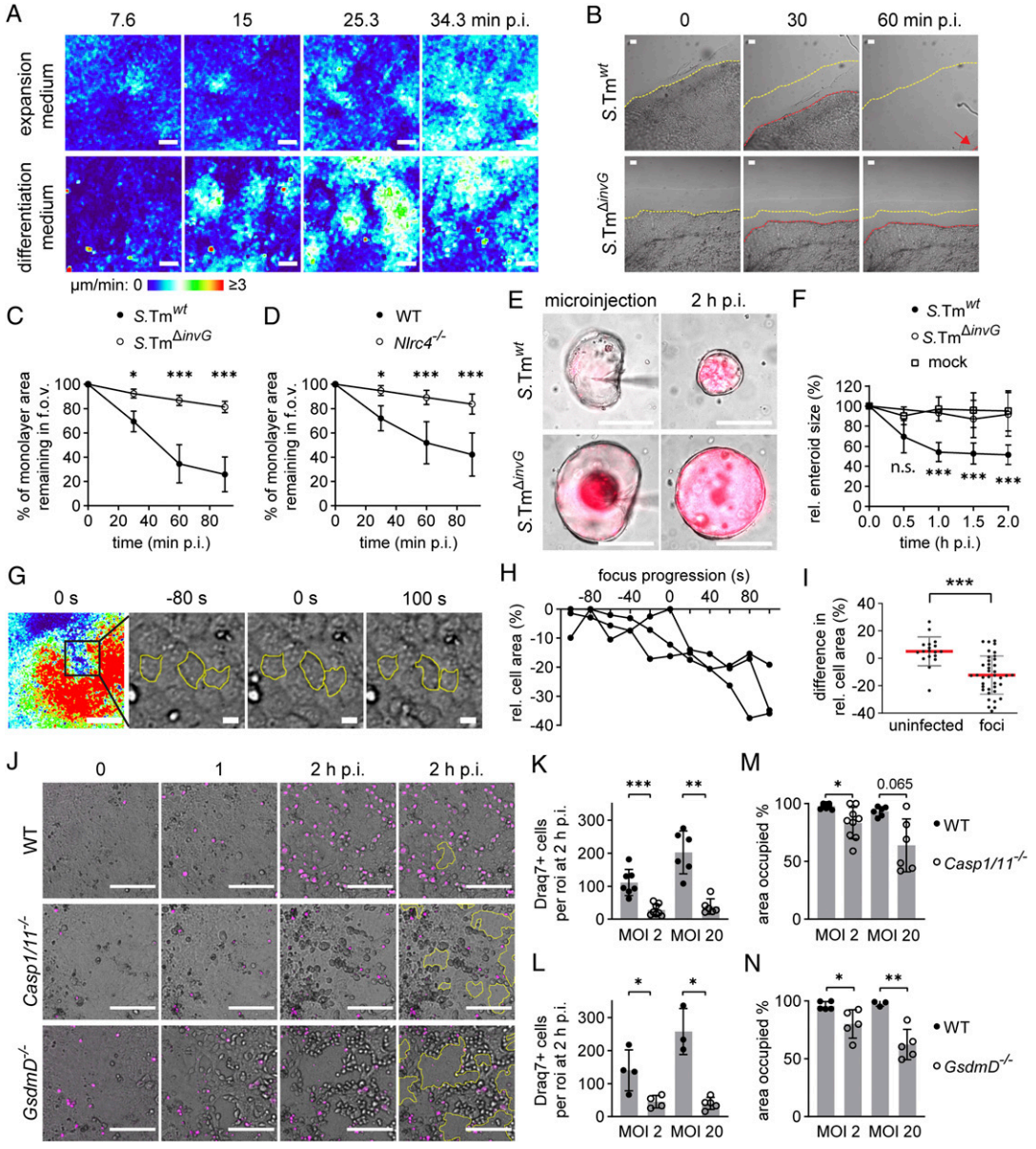

Fig. 5. Focal contractions compact the epithelial layer and may prevent disintegration. (*A*) Human enteroid-derived IEC monolayers were generated atop Collagen-1 hydrogels and cultured in expansion medium or differentiation medium (see *SI Appendix, Materials and Methods* for details). Depicted are representative speed–color maps from time-lapse imaging of monolayers infected with *S*.Tm^{wt} at MOI 2 (time points on top). (Scale bars, 100 µm.) (*B* and *C*) Murine WT IEC monolayers (as in Fig. 1*A*, 72h p.s.) were detached from the culture chamber wall and infected with *S*.Tm^{wt} or *S*.Tm$^{\Delta invG}$. (*B*) DIC images at the edge of the monolayer (time points on top). Dashed lines represent the monolayer edge location at 0 (yellow), 30, and 60 min p.i. (red). (Scale bars, 100 µm.) (*C*) Quantification of the percentage of the monolayer area remaining in the f.o.v. (as in *B*). Data presented as mean ± SD of five monolayers, pooled from three independent experiments. (*D*) Quantification as in *C* of WT and *Nlrc4*$^{-/-}$ monolayers infected with *S*.Tm^{wt}. Data pooled from seven monolayers from three independent experiments. In *C–D*, two-way ANOVA with TukeyHSD was performed (**P* < 0.05; ****P* < 0.001). (*E* and *F*) Murine 3D-enteroids were microinjected with mCherry-*S*.Tm^{wt} or mCherry-*S*.Tm$^{\Delta invG}$. (*E*) DIC plus fluorescence image overlays (*S*.Tm in magenta) at the indicated time points of the time-lapse imaging series. (Scale bars, 100 µm.) (*F*) Quantification of enteroid size (cross-section area) after microinjection of *S*.Tm^{wt}, *S*.Tm$^{\Delta invG}$, or mock, as in *E*. Data presented as mean ± SD of ≥8 enteroids per condition, pooled from four independent experiments. Two-way ANOVA with TukeyHSD, comparing *S*.Tm^{wt} to mock, was performed (n.s., nonsignificant; ****P* < 0.001). (*G*) Representative speed–color map (*Left*) and blow-up DIC images (*Right*) from an *S*.Tm-elicited contraction focus at the indicated time points (seconds before/after maximum speed of contraction pulse). Yellow lines indicate outlines of three IECs. (Scale bars, 100 or 10 µm in speed–color map or DIC images, respectively.) (*H*) Relative cell area to maximal area over time for IECs outlined in *G*. (*I*) Quantification of individual IEC area change within contraction foci in *S*.Tm-infected monolayers (before and after maximal speed of contraction pulse compared) and in randomly picked regions of uninfected monolayers within the same time frame. Each dot represents one IEC. Mean ± SD depicted by red lines and error bars. Data pooled from three independent experiments. Two-tailed Mann–Whitney *U* test was performed (****P* < 0.001). (*J*) Representative time-lapse series of murine WT, *Casp1/11*$^{-/-}$, and *GsdmD*$^{-/-}$ monolayers infected with *S*.Tm^{wt} at MOI 2 in presence of Draq7 (magenta). Yellow lines indicate gaps in the monolayer. (Scale bars, 100 µm.) (*K* and *L*) Quantification of Draq7-positive cells at 2 h p.i. in *K* WT and *Casp1/11*$^{-/-}$ monolayers, or *L* WT and *GsdmD*$^{-/-}$ monolayers, infected in parallel at the indicated MOIs. (*M* and *N*) Quantification of area occupied by *M* WT and *Casp1/11*$^{-/-}$ monolayers, or *N* WT and *GsdmD*$^{-/-}$ monolayers, at 2 h p.i. with the indicated MOIs. In *K–N*, each dot represents one monolayer. Bars indicate mean ± SD. Data pooled from ≥3 independent experiments in each case. One-tailed Mann–Whitney *U* test in *K* and *L* and two-tailed Mann–Whitney *U* test in *M* and *N* were performed (**P* < 0.05; ***P* < 0.01; ****P* < 0.001, exact *P* value given in *M*).

addressed this possibility, first by measuring the retraction of the murine monolayer edge, after manually detaching it from the chamber wall prior to infection. Infection with *S*.Tm^{wt} produced an edge retraction in WT monolayers already within the first ~30 to 60 min p.i. (Fig. 5 *B* and *C*). By contrast, only negligible edge retraction was observed in response to noninvasive *S*.Tm$^{\Delta invG}$ (Fig. 5 *B* and *C*) or when *Nlrc4*$^{-/-}$ monolayers were infected with *S*.Tm^{wt} (Fig. 5*D*).

To explore the consequences of the 3D epithelial geometry found in the intact gut, we next microinjected *S*.Tm into the lumen of murine 3D-enteroids and followed the epithelial behavior by DIC imaging. In line with observations from monolayers, focal contractions were visible in infected 3D-enteroids. Strikingly, microinjection of *S*.Tm^{wt}, but not *S*.Tm$^{\Delta invG}$ or mock, resulted in a reduction of the total enteroid size by ~25 to 50% during the first 30 to 60 min p.i. (Fig. 5 *E* and *F*). This shows that *S*.Tm infection causes prompt compaction also of 3D-arranged murine epithelia.

As shown here and previously (12, 15, 16), *S*.Tm infection causes death and removal of infected IECs. We hypothesized that prompt and early focal contractions may prepare the epithelium to withstand the effects of subsequent IEC loss. Indeed, focal contractions led to an increased IEC packing in the affected regions, as evident from an up to 40% (mean 12.3%) reduction in the surface area of individual IECs (Fig. 5 *G*–*I*). To further test our hypothesis, we exploited the fact that Caspase-1– or Gasdermin D–deficient IECs still undergo NAIP/NLRC4–dependent cell death and expulsion (*SI Appendix*, Fig. S3*B* and refs. 12, 47) but that monolayers from these genetic backgrounds fail to elicit focal, epithelium-compacting, contractions (Fig. 4 *A*–*D*). WT, *Casp1/11*$^{-/-}$, and *GsdmD*$^{-/-}$ monolayers were infected with *S*.Tm^{wt} and imaged for a period extending beyond the contraction phase (i.e., for 2 h). As expected, *Casp1/11*$^{-/-}$ and *GsdmD*$^{-/-}$ monolayers produced fewer Draq7-positive IECs than WT controls at the end of the imaging series (Fig. 5 *J*–*L*), but we still observed expelling (mostly Draq7-negative) IECs (Fig. 5*J* and *SI Appendix*, Fig. S3*B*). Remarkably, despite the attenuated IEC death response, both *Casp1/11*$^{-/-}$ and *GsdmD*$^{-/-}$ monolayers lost epithelium integrity to a higher degree than WT controls (Fig. 5 *M* and *N*). At the end of the imaging series, intact WT monolayer still covered ≥93% of the infected areas, whereas *Casp1/11*$^{-/-}$ and *GsdmD*$^{-/-}$ monolayers displayed frequent gaps and covered a mean of 62 to 83% of the surface depending on the MOI (Fig. 5 *M* and *N*).

Taken together, these data associate early NAIP/NLRC4/Caspase-1/Gasdermin D/myosin–dependent focal contractions with increased local IEC packing and an enhanced capacity of the epithelium to withstand the potentially disruptive effects of subsequent IEC loss.

Discussion

Defense systems that protect the gut mucosa from infection can be broadly categorized into preexisting homeostatic barriers (e.g., the mucus layer and baseline levels of antimicrobial peptide and soluble IgA secretion) and responses elicited upon pathogen sensing (e.g., proinflammatory cytokine production, immune cell recruitment, and epithelial cell death). The homeostatic barriers are permanently in place but generic in nature. The elicited responses, on the other hand, can be tailored to best counter the invading pathogen but require time—in some cases hours to days—for full effect. This is especially true if they involve communication between multiple cell types. Here, we have uncovered a prompt and autonomous epithelial contraction response, which takes place in the absence of IEC—immune cell cross-talk. Occurring already within minutes of bacterial encounter, this may constitute one of the earliest elicited responses to gut mucosa infection.

Using bacterial and mammalian genetics, we find that sensing of TTSS and/or flagellin at pathogen invasion sites by epithelial NAIP/NLRC4 elicits the focal contractions. This response is still operational in the absence of ASC, which excludes an essential role of this adapter protein and its downstream interaction partners (e.g., Caspase-8 [12, 47]) in the execution. Instead, our data support that minute amounts of activated Caspase-1 and Gasdermin D cause sublytic pore formation, ion fluxes, and the swift propagation of a focal myosin-dependent contraction from the NAIP/NLRC4 sensing event at the epicenter. Importantly, multiple lines of evidence demonstrate that the contraction response precedes and can be uncoupled from previously described effects of IEC inflammasome activation, namely epithelial cell death, the IEC extrusion process, and generalized proinflammatory signaling (12, 13, 15, 16, 55): 1) NAIP/NLRC4–dependent contraction foci emerge before the expulsion and lysis of infected IECs, 2) broad-spectrum Caspase-inhibitor treatment dramatically reduces epithelial cell death without affecting the contraction response, and 3) we identify at least two conditions (homeostatic IEC removal in WT epithelia and infection-induced IEC removal in *Casp1/11*$^{-/-}$ or *GsdmD*$^{-/-}$ epithelia) in which IEC death and expulsion occurs in the absence of a contraction response. It is here especially noteworthy that an actin purse string forms in neighboring epithelial cells both during IEC expulsion initiated by NLRC4/Caspase-1/Gasdermin D, by NLRC4/ASC/Caspase-8 (12), and in non-infection–related cell extrusion (50), while the contraction response described here only occurs in the first case and in an earlier time window. Moreover, 4) a range of inhibitor, neutralization, and supernatant transfer experiments argue against a central contribution by released mediators. Finally, 5) both TTSS-1–proficient and –deficient *S*.Tm trigger generalized proinflammatory gene expression in the epithelium, whereas only TTSS-1–proficient *S*.Tm elicit contraction foci. Taken together, these observations also distinguish the focal contraction response from previously described modes of cell-to-cell amplification of inflammatory signaling in bacteria-infected epithelia (18, 19). We cannot, however, refute that so far, unknown soluble mediator(s) or other forms of intercellular communication beyond what we report here may contribute to contraction focus propagation.

Nevertheless, our combined results support a central role for sublytic Gasdermin D pores that allow ion fluxes (including Calcium) to induce swift non-muscle myosin II–driven contractions that propagate from the focal epicenters. The nature of the propagation step remains poorly defined and could involve both chemical and physical transducers. Biophysical propagation of actomyosin contractions, with myosin itself acting as both a force generator and mechanosensor at adherence junctions, has been described in other settings (53, 56, 57). Actomyosin machineries impact many aspects of epithelial function, including tissue growth and morphogenesis (53, 58), which is also true for the gut epithelium. Assemblies of actomyosin, for instance, drive the apical constriction that promotes crypt formation in enteroids (54). In our monolayer experiments, small focal contractions occasionally occurred, although at exceedingly rare frequency, also in the absence of infection. It is appealing to speculate that coupling a PRR pathway to an already existing actomyosin contraction circuit allows the gut epithelium to use a similar machinery for tissue-shaping and in the acute response to infection. In monocytes/macrophages, there is precedence for coupling of inflammasome signaling and regulation of the actin cytoskeleton (59–61), although the molecular wiring appears dissimilar to what we describe here.

It is noteworthy that epithelial contractions appeared most vigorous in murine epithelia, less pronounced in human epithelia, and were nondetectable in the cell lines Caco-2 C2Bbe1 and m-ICc$_{12}$ placed atop the same hydrogel. This might be due to the fact that diverse epithelial cells bind unequally to the matrix, which could impact cell–cell junction maturity, mechanosensing, or force generation. However, it appears more likely that differential

expression of inflammasome components provides the explanation. Primary murine IECs express high levels of NAIP1-6, NLRC4, and Caspase-1 (8, 9, 16, 42). Human IECs also express the sole human NAIP (http://www.proteinatlas.org/ENSG00000249437-NAIP), but in addition, a noncanonical Caspase-4 inflammasome impacts the human IEC response to *S*.Tm (13, 55). The mouse Caspase-4 ortholog, Caspase-11, has a neglectable effect in naïve IECs and requires inflammatory priming for full expression (9, 16, 42, 62). Transformed/immortalized epithelial cell lines feature low or even undetectable expression levels of NAIP1-6, NLRC4, and Caspase-1 (9, 13). Hence, high expression of NAIP/NLRC4 inflammasome components permit primary epithelia, and in particular primary murine epithelia, to sense bacterial invasion and elicit epithelial contractions.

Several beneficial effects of the epithelial contraction response can be pictured. First, monolayers incapable of producing contraction foci but still capable of eliciting IEC death and expulsion (i.e., *Casp1/11*$^{-/-}$ and *GsdmD*$^{-/-}$ backgrounds) lost epithelial layer integrity to a larger extent than WT counterparts. It appears plausible that a denser packing allows the epithelium to better withstand accelerated rates of local IEC loss, thereby preserving overall tissue integrity. Second, the early densification of the epithelium may in fact simplify the IEC expulsion response itself, as local crowding in other contexts has been shown to promote dislodging of both dying and live cells from confluent cell layers (63). Third, we have recently found that *S*.Tm preferentially invades IECs at apicolateral hotspots close to IEC–IEC junctions (38). A local densification of the epithelium is likely to decrease pathogen access to such preferred invasion sites following sensing of a pioneer intruder. Finally, we speculate that focal contractions might convey alert signals across larger areas of the gut epithelium. For instance, a subset of enteroendocrine IECs respond to mechanical force through the channel Piezo2 and release serotonin to increase muscular contraction and fluid secretion (64, 65). It is possible that such a responder circuit could couple early local contraction foci in the epithelium to organ-wide changes in gut motility at a later stage of an infection. These possibilities constitute intriguing areas for future inquiry.

In conclusion, this work has uncovered a prompt and coordinated epithelial contraction response to bacterial invasion, which precedes other established host response mechanisms and has gone unnoticed in cell line infection experiments. We anticipate that the possibilities provided by organoid technology and tissue engineering will pave the way for an improved understanding of this and other complex primary cell and tissue behaviors.

Materials and Methods

Ethical Statement. Human enteroid cultures were established from tissue resected from the proximal small bowel during bariatric surgery. Written informed consent was obtained from each subject. All personal data were pseudonymized before reaching the laboratory. The procedures were approved by the local governing body, Regionala Etikprövningsnämnden, Uppsala, Sweden, license number 2010–157 with addendum 2010–157-1 (2018-06-13). Procedures for keeping of laboratory mice and tissue harvesting were approved by the Kantonales Veterinäramt Zürich, Switzerland, approval no. 193/2016, or by Umeå Regionala Djurförsöksetiska Nämnd, Sweden, approval no. A25-2019, and were performed in accordance with the legal regulations.

A detailed description of bacterial strains and plasmids, FlaTox expression and purification, murine and human enteroid culture, 2D monolayer establishment, epithelial cell line culture, RT-qPCR analysis, infection conditions and chemicals, time-lapse microscopy, immunofluorescence, microinjection, and image analysis can be found in *SI Appendix*.

Statistical Analysis. Where applicable, statistical significance was assessed by the Kruskal Wallis with Dunn´s post hoc test and Benjamini-Hochberg correction, the Mann–Whitney *U* test, the χ^2 test, or the two-way ANOVA with Tukey's HSD (Honest Significant Difference), as indicated in the figure legends. Tests were performed in GraphPad Prism (8.4.2) or in R studio.

Data Availability. All study data are included in the article and/or supporting information.

ACKNOWLEDGMENTS. We thank members of the Sellin laboratory for helpful discussions. We are grateful to the staff of the Biological Visualization platform, Uppsala University, for instrument access, to the staff at Samariterhemmet surgical unit, Department of Surgery, Uppsala University Hospital, for assistance with human intestinal tissue sampling, and to Hui Jiang, Umeå University, for assistance with murine intestinal tissue sampling. Tim Keys is acknowledged for advice on protein purification. W.D.H. acknowledges financial support by the Swiss National Science Foundation (310030_192567). Work in the Sellin laboratory was supported by the SciLifeLab Fellows program, grants from the Swedish Research Council (2018-02223), the Swedish Foundation for Strategic Research (ICA16-0031, FFL18-0165), the Knut and Alice Wallenberg Foundation (2016.0063), and a Lennart Philipson Award to M.E.S.

1. P. R. Kiela, F. K. Ghishan, Physiology of intestinal absorption and secretion. *Best Pract. Res. Clin. Gastroenterol.* **30**, 145–159 (2016).
2. H. F. Helander, L. Fändriks, Surface area of the digestive tract–Revisited. *Scand. J. Gastroenterol.* **49**, 681–689 (2014).
3. A. C. Luissint, C. A. Parkos, A. Nusrat, Inflammation and the intestinal barrier: Leukocyte-epithelial cell interactions, cell junction remodeling, and mucosal repair. *Gastroenterology* **151**, 616–632 (2016).
4. S. A. Fattinger, M. E. Sellin, W.-D. Hardt, Epithelial inflammasomes in the defense against Salmonella gut infection. *Curr. Opin. Microbiol.* **59**, 86–94 (2021).
5. W. I. Khan, S. M. Collins, Gut motor function: Immunological control in enteric infection and inflammation. *Clin. Exp. Immunol.* **143**, 389–397 (2006).
6. A. E. Price *et al*., A map of Toll-like receptor expression in the intestinal epithelium reveals distinct spatial, cell type-specific, and temporal patterns. *Immunity* **49**, 560–575.e6 (2018).
7. M. E. Sellin, K. M. Maslowski, K. J. Maloy, W.-D. Hardt, Inflammasomes of the intestinal epithelium. *Trends Immunol.* **36**, 442–450 (2015).
8. N. Winsor, C. Krustev, J. Bruce, D. J. Philpott, S. E. Girardin, Canonical and noncanonical inflammasomes in intestinal epithelial cells. *Cell. Microbiol.* **21**, e13079 (2019).
9. A. Hausmann *et al*., Germ-free and microbiota-associated mice yield small intestinal epithelial organoids with equivalent and robust transcriptome/proteome expression phenotypes. *Cell. Microbiol.* **22**, e13191 (2020).
10. B. He *et al*., Intestinal bacteria trigger T cell-independent immunoglobulin A(2) class switching by inducing epithelial-cell secretion of the cytokine APRIL. *Immunity* **26**, 812–826 (2007).
11. S. Hu *et al*., The DNA sensor AIM2 maintains intestinal homeostasis via regulation of epithelial antimicrobial host defense. *Cell Rep.* **13**, 1922–1936 (2015).
12. I. Rauch *et al*., NAIP-NLRC4 inflammasomes coordinate intestinal epithelial cell expulsion with eicosanoid and IL-18 release via activation of caspase-1 and -8. *Immunity* **46**, 649–659 (2017).
13. M. K. Holly *et al*., Salmonella enterica infection of murine and human enteroid-derived monolayers elicits differential activation of epithelium-intrinsic inflammasomes. *Infect. Immun.* **88**, e00017-20 (2020).
14. K. Brandl, G. Plitas, B. Schnabl, R. P. DeMatteo, E. G. Pamer, MyD88-mediated signals induce the bactericidal lectin RegIII γ and protect mice against intestinal Listeria monocytogenes infection. *J. Exp. Med.* **204**, 1891–1900 (2007).
15. L. A. Knodler *et al*., Dissemination of invasive Salmonella via bacterial-induced extrusion of mucosal epithelia. *Proc. Natl. Acad. Sci. U.S.A.* **107**, 17733–17738 (2010).
16. M. E. Sellin *et al*., Epithelium-intrinsic NAIP/NLRC4 inflammasome drives infected enterocyte expulsion to restrict Salmonella replication in the intestinal mucosa. *Cell Host Microbe* **16**, 237–248 (2014).
17. L. V. Hooper, Epithelial cell contributions to intestinal immunity. *Adv. Immunol.* **126**, 129–172 (2015).
18. T. Dolowschiak *et al*., Potentiation of epithelial innate host responses by intercellular communication. *PLoS Pathog.* **6**, e1001194 (2010).
19. C. A. Kasper *et al*., Cell-cell propagation of NF-κB transcription factor and MAP kinase activation amplifies innate immunity against bacterial infection. *Immunity* **33**, 804–816 (2010).
20. A. L. Chang-Graham *et al*., Rotavirus induces intercellular calcium waves through ADP signaling. *Science* **370**, eabc3621 (2020).
21. K. Kretzschmar, H. Clevers, Organoids: Modeling development and the stem cell niche in a dish. *Dev. Cell* **38**, 590–600 (2016).
22. T. Sato *et al*., Single Lgr5 stem cells build crypt-villus structures in vitro without a mesenchymal niche. *Nature* **459**, 262–265 (2009).
23. H. Miyoshi, T. S. Stappenbeck, In vitro expansion and genetic modification of gastrointestinal stem cells in spheroid culture. *Nat. Protoc.* **8**, 2471–2482 (2013).
24. C. Moon, K. L. VanDussen, H. Miyoshi, T. S. Stappenbeck, Development of a primary mouse intestinal epithelial cell monolayer culture system to evaluate factors that modulate IgA transcytosis. *Mucosal Immunol.* **7**, 818–828 (2014).

25. J. In *et al*., Enterohemorrhagic *Escherichia coli* reduce mucus and intermicrovillar bridges in human stem cell-derived colonoids. *Cell. Mol. Gastroenterol. Hepatol.* **2**, 48–62.e3 (2016).
26. Y. Wang *et al*., Self-renewing monolayer of primary colonic or rectal epithelial cells. *Cell. Mol. Gastroenterol. Hepatol.* **4**, 165–182.e7 (2017).
27. K. Kozuka *et al*., Development and characterization of a human and mouse intestinal epithelial cell monolayer platform. *Stem Cell Reports* **9**, 1976–1990 (2017).
28. T. Sato *et al*., Long-term expansion of epithelial organoids from human colon, adenoma, adenocarcinoma, and Barrett's epithelium. *Gastroenterology* **141**, 1762–1772 (2011).
29. I. Heo *et al*., Modelling Cryptosporidium infection in human small intestinal and lung organoids. *Nat. Microbiol.* **3**, 814–823 (2018).
30. J. Y. Co *et al*., Controlling epithelial polarity: A human enteroid model for host-pathogen interactions. *Cell Rep.* **26**, 2509–2520.e4 (2019).
31. J. Zhou *et al*., Infection of bat and human intestinal organoids by SARS-CoV-2. *Nat. Med.* **26**, 1077–1083 (2020).
32. P. Geiser *et al*., Salmonella enterica serovar typhimurium exploits cycling through epithelial cells to colonize human and murine enteroids. *mBio* **12**, e02684-20 (2021).
33. X. Yin *et al*., Niche-independent high-purity cultures of Lgr5+ intestinal stem cells and their progeny. *Nat. Methods* **11**, 106–112 (2014).
34. G. Altay *et al*., Self-organized intestinal epithelial monolayers in crypt and villus-like domains show effective barrier function. *Sci. Rep.* **9**, 1–14 (2019).
35. J. Eriksson, D. Styrström, M. E. Sellin, Cellocity: A Python package for analysis of confluent cell layer dynamics. *J. Open Source Softw.* **6**, 2818 (2021).
36. J. E. Galán, R. Curtiss III, Cloning and molecular characterization of genes whose products allow Salmonella typhimurium to penetrate tissue culture cells. *Proc. Natl. Acad. Sci. U.S.A.* **86**, 6383–6387 (1989).
37. M. Furter, M. E. Sellin, G. C. Hansson, W.-D. Hardt, Mucus architecture and near-surface swimming affect distinct Salmonella typhimurium infection patterns along the murine intestinal tract. *Cell Rep.* **27**, 2665–2678.e3 (2019).
38. S. A. Fattinger *et al*., Salmonella Typhimurium discreet-invasion of the murine gut absorptive epithelium. *PLoS Pathog.* **16**, e1008503 (2020).
39. C. M. Collazo, J. E. Galán, The invasion-associated type III system of Salmonella typhimurium directs the translocation of Sip proteins into the host cell. *Mol. Microbiol.* **24**, 747–756 (1997).
40. P. J. Hume, V. Singh, A. C. Davidson, V. Koronakis, Swiss army pathogen: The *Salmonella* entry toolkit. *Front. Cell. Infect. Microbiol.* **7**, 348 (2017).
41. K. Zhang *et al*., Minimal SPI1-T3SS effector requirement for Salmonella enterocyte invasion and intracellular proliferation in vivo. *PLoS Pathog.* **14**, e1006925 (2018).
42. A. Hausmann *et al*., Intestinal epithelial NAIP/NLRC4 restricts systemic dissemination of the adapted pathogen Salmonella Typhimurium due to site-specific bacterial PAMP expression. *Mucosal Immunol.* **13**, 530–544 (2020).
43. S. Mariathasan *et al*., Differential activation of the inflammasome by caspase-1 adaptors ASC and Ipaf. *Nature* **430**, 213–218 (2004).
44. J. von Moltke *et al*., Rapid induction of inflammatory lipid mediators by the inflammasome in vivo. *Nature* **490**, 107–111 (2012).
45. I. Rauch *et al*., NAIP proteins are required for cytosolic detection of specific bacterial ligands in vivo. *J. Exp. Med.* **213**, 657–665 (2016).
46. J. Ding *et al*., Pore-forming activity and structural autoinhibition of the gasdermin family. *Nature* **535**, 111–116 (2016).
47. N. Van Opdenbosch *et al*., Caspase-1 engagement and TLR-induced c-FLIP expression suppress ASC/Caspase-8-dependent apoptosis by inflammasome sensors NLRP1b and NLRC4. *Cell Rep.* **21**, 3427–3444 (2017).
48. P. Li *et al*., Mice deficient in IL-1 β-converting enzyme are defective in production of mature IL-1 β and resistant to endotoxic shock. *Cell* **80**, 401–411 (1995).
49. J. Shi *et al*., Cleavage of GSDMD by inflammatory caspases determines pyroptotic cell death. *Nature* **526**, 660–665 (2015).
50. J. Rosenblatt, M. C. Raff, L. P. Cramer, An epithelial cell destined for apoptosis signals its neighbors to extrude it by an actin- and myosin-dependent mechanism. *Curr. Biol.* **11**, 1847–1857 (2001).
51. Y. Gu, T. Forostyan, R. Sabbadini, J. Rosenblatt, Epithelial cell extrusion requires the sphingosine-1-phosphate receptor 2 pathway. *J. Cell Biol.* **193**, 667–676 (2011).
52. H. M. Russo *et al*., Active caspase-1 induces plasma membrane pores that precede pyroptotic lysis and are blocked by lanthanides. *J. Immunol.* **197**, 1353–1367 (2016).
53. A. C. Martin, B. Goldstein, Apical constriction: Themes and variations on a cellular mechanism driving morphogenesis. *Development* **141**, 1987–1998 (2014).
54. L. Hartl, G. Huelsz-Prince, J. van Zon, S. J. Tans, Apical constriction is necessary for crypt formation in small intestinal organoids. *Dev. Biol.* **450**, 76–81 (2019).
55. L. A. Knodler *et al*., Noncanonical inflammasome activation of caspase-4/caspase-11 mediates epithelial defenses against enteric bacterial pathogens. *Cell Host Microbe* **16**, 249–256 (2014).
56. M. J. Greenberg, G. Arpağ, E. Tüzel, E. M. Ostap, A perspective on the role of myosins as mechanosensors. *Biophys. J.* **110**, 2568–2576 (2016).
57. E. Sadeghipour, M. A. Garcia, W. J. Nelson, B. L. Pruitt, Shear-induced damped oscillations in an epithelium depend on actomyosin contraction and E-cadherin cell adhesion. *eLife* **7**, e39640 (2018).
58. L. He, X. Wang, H. L. Tang, D. J. Montell, Tissue elongation requires oscillating contractions of a basal actomyosin network. *Nat. Cell Biol.* **12**, 1133–1142 (2010).
59. A. L. Waite *et al*., Pyrin and ASC co-localize to cellular sites that are rich in polymerizing actin. *Exp. Biol. Med. (Maywood)* **234**, 40–52 (2009).
60. A. Akhter *et al*., Caspase-11 promotes the fusion of phagosomes harboring pathogenic bacteria with lysosomes by modulating actin polymerization. *Immunity* **37**, 35–47 (2012).
61. S. M. Man *et al*., Actin polymerization as a key innate immune effector mechanism to control Salmonella infection. *Proc. Natl. Acad. Sci. U.S.A.* **111**, 17588–17593 (2014).
62. S. M. Crowley *et al*., Intestinal restriction of Salmonella Typhimurium requires caspase-1 and caspase-11 epithelial intrinsic inflammasomes. *PLoS Pathog.* **16**, e1008498 (2020).
63. G. T. Eisenhoffer *et al*., Crowding induces live cell extrusion to maintain homeostatic cell numbers in epithelia. *Nature* **484**, 546–549 (2012).
64. C. Alcaino *et al*., A population of gut epithelial enterochromaffin cells is mechanosensitive and requires Piezo2 to convert force into serotonin release. *Proc. Natl. Acad. Sci. U.S.A.* **115**, E7632–E7641 (2018).
65. G. M. Mawe, J. M. Hoffman, Serotonin signalling in the gut–Functions, dysfunctions and therapeutic targets. *Nat. Rev. Gastroenterol. Hepatol.* **10**, 473–486 (2013).